PHYSICAL REVIEW E **96**, 053202 (2017)

Experimental determination of phase transitions by means of configurational entropies in finite Yukawa balls

Matthias Mulsow and André Melzer
Institut für Physik, Ernst-Moritz-Arndt-Universität Greifswald, 17489 Greifswald, Germany
(Received 19 September 2017; published 9 November 2017)

The phase transition of finite Yukawa balls (ordered systems of microspheres in a gaseous plasma environment) with less than 100 particles is studied experimentally by means of configurational entropies. We have developed cylindrical two- and three-particle-correlation functions to measure these entropies for multiple cluster sizes over a wide temperature range. The cluster temperature is finely tuned using a stochastic laser heating setup. It is shown that the correlation functions give a detailed insight into the structural properties of the cluster. The derived configurational entropies give a clear indication of the transition temperature from a solid-like to a fluid-like state. Comparing the transition temperatures of different sized clusters it is found that the transition temperature increases with cluster size in general agreement with theoretical predictions.

DOI: 10.1103/PhysRevE.96.053202

I. INTRODUCTION

The transition from very small clusters with only few constituents to an extended system is essential for the understanding of how macroscopic effects of matter develop on multiple scales. Well-known objects of investigation for these effects are, e.g., atomic and molecular clusters [1–3] or the many forms of granular matter [4]. Such systems inherit properties that depend on the number of constituents and how they interact on the individual level. The focus of this work will be on the determination of phase transitions of rather small conglomerates and how they are affected by the number of constituents.

The objects of investigation in this paper are Yukawa balls in a dusty plasma environment. Besides the neutral gas component, dusty plasmas consist of ions and electrons with an additional third charged species, the dust (for details, see, e.g., [5–7] and related references therein). These macroscopic dust particles with a size between a few nanometers and several micrometers charge due to the inflow of plasma electrons and ions. Usually, they gain very high negative charges since the electrons are more mobile than the ions. Yukawa balls [8–11] are finite three-dimensional systems made of only a few to thousands of microspheres. From the competition of Coulomb repulsion and confining plasma forces the particles arrange in a spherical structure on nested, concentric shells [12,13]. Being strongly coupled but optically thin makes them a unique and rich tool for investigating size-depending effects of phase transitions on the individual particle level. In such a finite particle system one can directly measure the velocity v of individual particles with mass m. From that one can define the kinetic temperature $T = m\langle v^2\rangle/3k_\mathrm{B}$ of the system from the particles' velocity distribution. By increasing the kinetic temperature of the particles one can drive and study phase transitions in these small systems.

In a simplified picture the point of phase transition of a macroscopic solid state body can be determined by feeding heat to the system and monitor the temperature change. First, the temperature will rise as the atoms oscillate stronger around their fixed lattice positions. At a certain point the temperature rise will stop because the additional heat is used to break up the bond structure. This point is the transition temperature in a first-order phase transition. Upon further heating the atoms overcome their lattice positions entering the liquid state where the atoms can move more freely. Accordingly, the system exhibits a jump in the entropy at the transition temperature.

It is a question of high interest how this can be translated into a finite system of less than 100 charged particles that form an ordered structure like a Yukawa ball. A strongly coupled charged-particle system is described by the coupling parameter which is the ratio of thermal and Coulomb energy

$$\Gamma = \frac{Z^2 e^2}{4\pi\varepsilon_0 b_\mathrm{WS}} \frac{1}{k_\mathrm{B} T} \tag{1}$$

with the electrical charge number Z and the Wigner-Seitz distance $b_\mathrm{WS} = \sqrt[3]{3/4\pi n}$, which is of the order of the interparticle distance and is calculated from the particle number density n. It has been shown in simulations [14] that an infinite three-dimensional (3D) one-component plasma (a system of a single charged species in a homogeneous neutralizing background) will change its phase from solid to liquid at a critical value of $\Gamma_\mathrm{crit} \approx 168$ being solid above it and liquid-like below it. In an experimental dusty plasma the particles interact with a shielded Coulomb potential which affects the crystallization properties. To account for this, Ikezi [15] estimated a modified coupling parameter $\Gamma_\mathrm{eff,crit} = \Gamma\exp(-\kappa) = 168$ with an added shielding term $\kappa = b_\mathrm{WS}/\lambda_\mathrm{D}$ which gives the Wigner-Seitz radius in units of the Debye length λ_D. This has been studied further by Vaulina *et al.* [16] revealing a more complex dependency between coupling parameter and screening. However, in general the transition line for a Yukawa system runs in a $\Gamma - \kappa$-plane where the (unmodified) critical coupling parameter increases with the strength of the shielding [17].

Schiffer [18] studied in simulations how the critical coupling parameter depends on the number of particles for finite systems. He evaluated the transition temperature as an inverse coupling parameter for different sized Coulomb clusters. He has shown that the critical coupling parameter increases with the decreasing particle number.

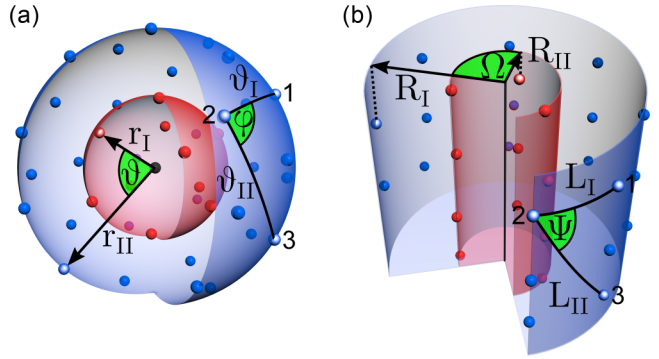

FIG. 1. Sketch of Yukawa clusters with two shells illustrating the coordinates used for the C2P and TCF in a) spherical symmetry and b) cylindrical symmetry.

The aim of this paper is to study the size dependence of the transition temperature for Yukawa balls with less than 100 particles. To reach it we want to induce and investigate phase transitions and identify the critical point by using statistical entropy methods.

II. CONFIGURATIONAL ENTROPIES

Phase transitions in finite systems can be described in a phenomenological way, for example by analyzing fluctuations in the calculated inter-particle distance [19] or by looking at the decay of radial and angular correlation functions [20–22]. Recently, a melting criterion has been derived from a thermodynamics quantity by Thomsen and Bonitz using configurational entropies from different particle correlation functions [23]. This allows identifying phase transitions in finite systems on a quantitative level and it is the aim of this paper to study these entropies from experiments.

Two correlation functions used by Thomsen and Bonitz are the *center two-particle correlation function* (C2P) and the *triple correlation function* (TCF) to measure the configurational entropy of a system. These correlations are evaluated from the 3D positions of the particles in a specific set of coordinates exploiting the spherical symmetry of the problem as illustrated in Fig. 1(a). For the C2P the length of the respective position vectors r_I and r_{II} relative to the trap center and the solid angle ϑ between them are considered. The TCF uses a particle triplet 1-2-3 on a selected shell evaluating the angular distances $\vartheta_I, \vartheta_{II}$ between particles 2-1 and 2-3 and the bond angle φ on the spherical shell surface.

For the C2P, the probability of finding a particle pair at r_I, r_{II}, and ϑ is determined by averaging over all particle pairs. Similarly, for the TCF the probability of finding particle triplets with $\vartheta_I, \vartheta_{II}$, and φ is determined. Moreover, the averaging extends over a large number of manifestations of the finite system at a fixed temperature. Hence, one needs the 3D positions of all particles at many instants in the described coordinate sets Q. This poses a challenge to the experiments. Finally, the space-resolved histograms $\tilde{\rho}_k(Q)$ have to be normalized by geometrical factors V_k that depend on the chosen coordinates and are given in [23] for spherical symmetry. Hence, the correlation functions are given as

$$\mathrm{C2P}(r_I, r_{II}, \vartheta) = \frac{\tilde{\rho}_2(r_I, r_{II}, \vartheta)}{V_2(r_I, r_{II}, \vartheta)} \tag{2}$$

and

$$\mathrm{TCF}(\vartheta_I, \vartheta_{II}, \varphi) = \frac{\tilde{\rho}_3(\vartheta_I, \vartheta_{II}, \varphi)}{V_3(\vartheta_I, \vartheta_{II}, \varphi)}, \tag{3}$$

where k indicates the number of correlated particles. From those, the reduced Shannon entropies

$$S^{(2)} \equiv -\langle \ln \mathrm{C2P} \rangle \quad \text{and} \quad S^{(3)} \equiv -\langle \ln \mathrm{TCF} \rangle \tag{4}$$

measure the configurational entropy of the system at the temperature T (see [23,24]). As usual, it is possible to derive heat capacities as $C = \partial S / \partial T$ but this paper will focus purely on the configurational entropy. The described correlation functions and configurational entropies have been investigated in simulations by Thomsen and Bonitz using Yukawa balls with perfect spherical symmetry.

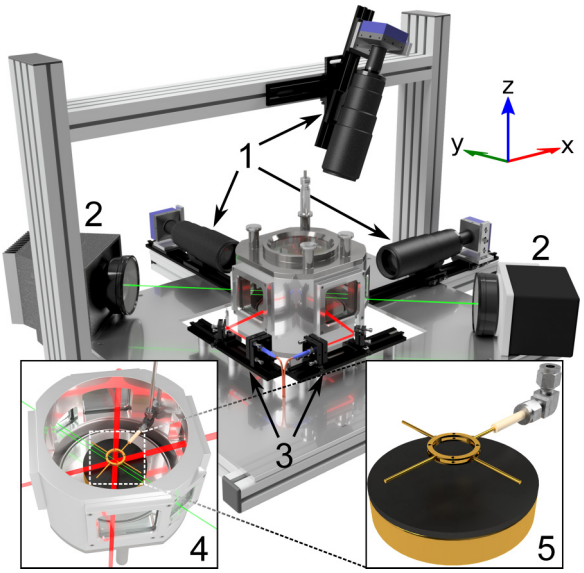

FIG. 2. Experimental setup: 1—CMOS cameras, 2—galvanometer scanners for laser manipulation, 3—illumination lasers, 4—rf plasma chamber, 5—confinement ring above heatable electrode.

III. EXPERIMENTAL SETUP

The experimental setup shown in Fig. 2 is a refined version of the one used by Schella *et al.* [22,25]. Its centerpiece is a capacitively coupled radio frequency (rf) discharge operated in argon at gas pressures typically between 5 and 50 Pa. The electrode at the bottom of the chamber is driven with rf powers below 2 W while the rest of the chamber is grounded, hence forming an asymmetrical low temperature discharge.

Melamine-formaldehyde (MF) particles with a radius of 4.7 μm are trapped in the sheath region above the rf-electrode. For confinement of the particles we use a brass ring instead of the conventional glass cuvette [10]. The ring floats electrically and is positioned about 20 mm above and parallel to the electrode. The upwards sheath electric field, the radial inwards electric field due to the ring and the downward gravitational field create a nearly harmonic 3D confinement in which the

particles form a Yukawa ball. The experiments on the dust clusters shown here have been performed at a gas pressure of 14.5 Pa and an rf power of 800 mW.

In order to observe the particles they are illuminated by two fiber-coupled DPSS lasers at 660 nm with a light output of up to 1000 mW each. The forward scattered light is captured by three CMOS cameras that record images at a resolution of 1280 × 1024 pixels at a frame rate of up to 500 fps. Two cameras are viewing from the side under 90° relative to each other, while the third is viewing from top, however slightly tilted by 22° with respect to the vertical direction. Camera calibration and epipolar-line particle reconstruction developed by Himpel *et al.* [26–28] based on the work of Wenger *et al.* [29] and Bouguet [30] has been applied to retrieve the 3D particle position from the individual camera images.

To investigate the phase transition of the Yukawa ball one needs to observe it at different temperatures. Established experimental methods to induce phase transitions [22,31–33] alter the neutral gas pressure, plasma power or particle number in dusty plasmas. These methods affect more than a single quantity in the coupling parameter. Furthermore they rely partly on additional instabilities due to ion streaming [34,35] which are not considered in the coupling parameter making it difficult to evaluate their impact on the phase transition. To overcome this we chose a pure laser heating setup to raise the kinetic energy of the particles directly via radiation pressure leaving the confining plasma system undisturbed [22,25,36–38]. The focused light of two green (532 nm) laser modules with up to 600 mW each is distributed over the cluster by two galvanometer scanners using random scan patterns. With the laser power the kinetic temperature of the particles is controlled. Increasing the laser power leads to higher particle temperatures, see [39] for details.

In the measurements, Yukawa balls with particle numbers from 17 to 72 are trapped and heated at various laser power settings. For each laser-driven temperature the motion of all particles is recorded over 5000 frames at 100 fps. The 3D particle positions have been reconstructed for all 5000 frames at a fixed temperature. From that the particle correlation functions and the corresponding configurational entropies are calculated as described in the following.

IV. RESULTS

A. Structure of Yukawa balls

The typical structure of Yukawa balls that we investigate in our experiment can be seen in Fig. 3(a) for an example of a 39-particle cluster, consisting of two shells. It can be seen that especially the particles of the inner shell are located atop of each other. Obviously, in the experimental environment streaming ions [34] lead to chain-like vertical particle alignment. Hence, it seems that the particles arrange in a cluster structure with a more cylindrical symmetry [35,40].

To illustrate this further, the particle density of the cluster is shown in Fig. 3(b). The density has been calculated from the particle positions as a mean over all frames. The density is shown averaged over the azimuthal angle Ω in cylindrical $R - Z$ coordinates where $R = \sqrt{X^2 + Y^2}$ is the radial coordinate and Z is the vertical direction (along gravity).

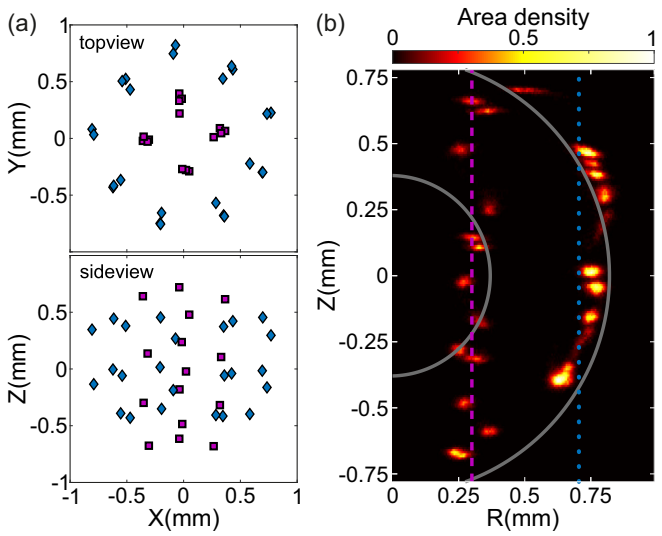

FIG. 3. (a) Particle positions retrieved from experimental data with indicated viewpoints and colored inner (magenta squares) and outer (blue diamonds) cylindrical shells. (b) Particle density as a function of radial and vertical coordinates R, Z averaged over the azimuthal angle Ω over 5000 frames. The lines indicate the projection of the spherical (solid gray) and cylindrical shells (inner: dashed magenta, outer: dotted blue).

For comparison, the circular solid lines indicate the expected positions when the particles would sit on two spherical shells. In contrast, the dashed and dotted lines indicate the situation for an arrangement on two cylinders. Obviously, none of the two symmetries matches the measured distribution perfectly since the cluster exhibits a chain-like structure in the center but is still somewhat spherically shaped in the outer layer. But in general, the cylindrical symmetry appears to be a much better reproduction of the structure of the cluster.

For the analysis of phase transitions in such systems the spherical C2P and TCF correlations seem not really adequate (see below). Therefore we have developed modified cylindrical versions of the C2P and TCF functions as shown in Fig. 1(b). The C2P now uses the radial cylindrical distances $R_\mathrm{I}, R_\mathrm{II}$ of two particles and the azimuth Ω between them with respect to the central Z-axis. Similar to the spherical version, the spherical TCF also works with a particle triple 1-2-3 except that it is now on a cylinder shell with the distances $L_\mathrm{I}, L_\mathrm{II}$ between particles 2-1 and 2-3 and the bond angle Ψ on the curved surfaces. Due to the symmetry change the geometrical factors V_k need to be recalculated as well [23]. For the cylindrical C2P we find $V_{2,\mathrm{cyl}} = 2\pi h^2 R_\mathrm{I} R_\mathrm{II}$, where h is the overall vertical length of the cluster. For the TCF we have chosen to sample this geometrical factor numerically due to the complexity of the Jacobi determinant.

To benchmark the modified correlations we computed the spherical and cylindrical version for various cluster sizes and temperatures. An exemplary visualization of the C2Ps can be seen in Fig. 4. Since the distributions depend on three coordinates, an integration over one coordinate is needed to provide a two dimensional representation. We follow Thomsen and Bonitz and integrate r_I over one of the shells, as indicated by black arrows in Fig. 4. Similarly for the cylindrical version

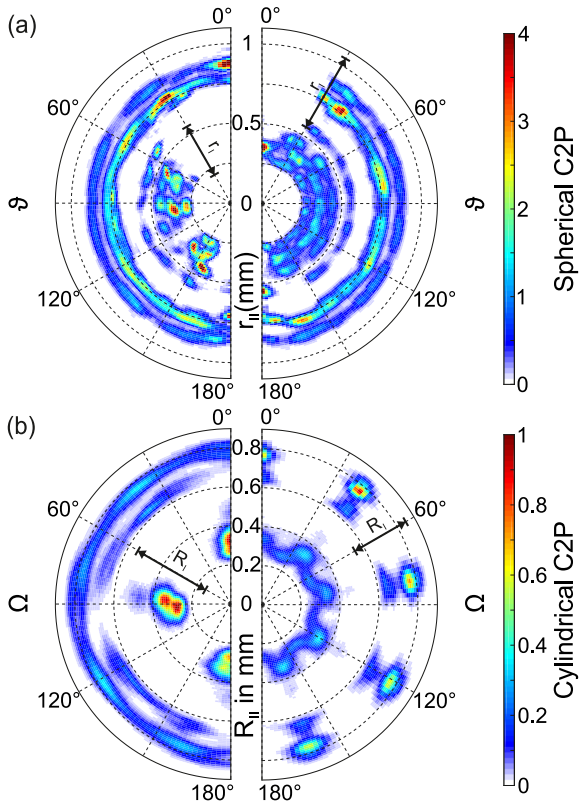

FIG. 4. Comparison of C2Ps with (a) spherical symmetry and (b) cylindrical symmetry computed for the 39-particle cluster shown in Fig. 3 at moderate heating ($\Gamma \approx 440$, solid state). To visualize the 3D distribution functions, they have been integrated over r_I and R_I, respectively, with borders in the range of the first shell (left hemispheres) and the second shell (right hemispheres) as indicated by the black arrows.

we chose to integrate R_I over one cylindrical shell. This results in as many 2D visualizations as there are shells where the first of the two correlated particles is always chosen from this particular shell.

We start with the discussion of the cylindrical C2P in Fig. 4(b). In the left hemisphere the C2P was integrated over the inner shell (where $0.2\,\text{mm} < R_I < 0.55\,\text{mm}$). This inner shell of the 39-particle cluster features four equidistant vertical particle chains (see Fig. 3), so an arbitrary particle on this shell will see other particles on the same shell at an angle Ω of about $0°$,$90°$, or $180°$. Correspondingly the C2P shows distinct islands of high correlation at these angles and a radius around $R_{II} \approx 0.3$ mm. The outer shell on the other hand features a nine-fold symmetry seen from above (see Fig. 3) which does not share a common divisor with the four-fold inner shell. This means the shells do not share a common symmetry and a particle on the first shell can see a particle on the second shell at various Ω resulting in the smeared out area at $R_{II} \approx 0.8$ mm. When we now look into the right hemisphere of Fig. 4(b), where the first particle was chosen to be in the outer shell ($0.55\,\text{mm} < R_I < 0.85\,\text{mm}$) we see high correlation in the outer shell at angles Ω of $0°$,$40°$,$80°$,$120°$ and $160°$ and at a radius of $R_{II} \approx 0.8$ mm in agreement with the nine-fold rotation symmetry. The inner shell now appears smeared out. We conclude that the cylindrical C2P represents the structure very well due to the rotational symmetry of the cluster seen from above.

Now, how does this compare to the spherical C2P shown in Fig. 4(a)? In both cases (where integrating over the inner spherical shell in the left hemisphere or the outer spherical shell in the right hemisphere) no clear correlations can be identified. In order to observe distinct correlation islands the cluster would need not only rotational symmetry around one axis but 3D isotropy which it lacks. So if one would try to analyze the evolution of a correlation island over a larger temperature range the finely structured spherical correlations would produce artifacts in the computed entropies. Similar behavior can be observed for the triple correlation function which will not be discussed in detail here. We therefore choose to use the cylindrical C2P and TCF to derive heat capacities and entropies for clusters of various particle numbers.

B. Correlation functions and heating

With the manipulation lasers, the cluster was heated in 26 steps from a kinetic temperature of 600 K up to 15000 K. The average particle charge number has been determined to be about $Z \approx 3400$ by normal mode analysis [41]. The Wigner-Seitz radius is measured as $b_{WS} = 0.28$ mm calculated from the static particle positions yielding a coupling parameter range between 1168 and 44. Hence, one should expect a phase transition happening inside that range.

At first the C2P and TCF distributions for a solid and a liquid phase state will be discussed. Starting with the C2P one can directly look into the changes due to the temperature increase since the structural properties that can be deducted for the solid case of $\Gamma \approx 440$ [Fig. 5(a)] were already described in Sec. IV A. The C2P for the heated cluster with $\Gamma \approx 130$ is shown in Fig. 5(b). Again, the distribution was integrated over R_I in the range of the first shell (left hemisphere) or second shell (right hemisphere). It is apparent that for $\Gamma \approx 130$ the overall distribution is smeared out compared to the solid case ($\Gamma \approx 440$). More precisely on the one hand the space between the two radial shells is now "filled" as well, which means that it is now possible to find a particle between the shells. Nevertheless, the individual shells are easily identified. Moreover, correlation peaks can still be identified as in the solid state, however less pronounced. On the other hand one can see in the right hemisphere of Fig. 5(b) that the long range angular order of the outer shell gets lost for $\Omega > 90°$. This stepped heating behavior with earlier loss of orientational order followed shortly by the loss of radial order is well known for finite systems [22,42] and confirms the applicability of the C2P.

Moving on to the TCFs shown in Figs. 5(c) and 5(d) it is important to mind the differences to the C2P. While the C2P uses all particle pairs of the whole cluster and the plot hemispheres are generated due to integrating over different shells, the TCF uses particle triples on one specific shell. Therefore the hemispheres in Figs. 5(c) and 5(d) show different correlation functions for the two shells. Nevertheless it is still necessary to integrate over one of the variables to generate a 2D plot. Here we integrate over L_I with the range chosen so that the first and second particle are nearest neighbors. While the C2P polar plots can be interpreted as correlations from a top view

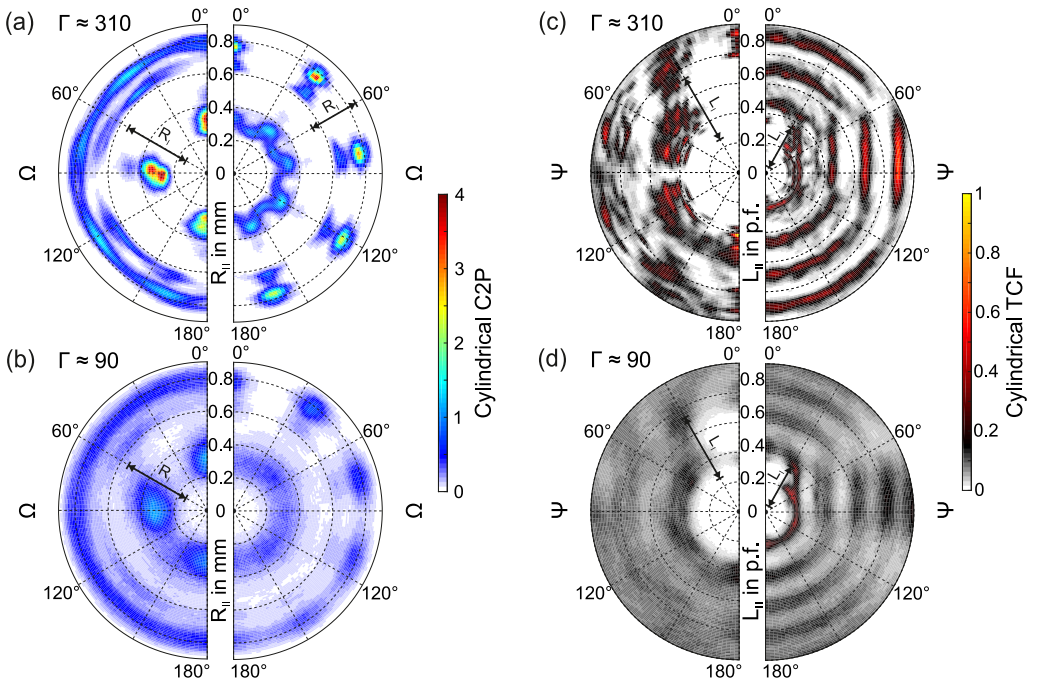

FIG. 5. Correlation functions for a 39-particle cluster in a solid state ($\Gamma \approx 440$) and in a liquid state ($\Gamma \approx 440$). (a),(b) Cylindrical C2P plots with integration borders in the range of the first shell (left hemispheres) and the second shell (right hemispheres) as indicated by the black arrows. (c),(d) Cylindrical TCF plots for the inner shell (left hemispheres) and the outer shell (right hemispheres). Integration borders for L_{I} have been chosen around the nearest neighbor distance as indicated by the black arrows.

on the clusters particle density the TCF show probable particle triplets on the unrolled cylinder side surface. Consequently, it is sufficient to have L_{II} in the range from 0 to half the perimeter of the cylindrical shell and Ψ in the range of 0 to 180°. Since the perimeter is different for the two shells, we normalize L_{II} to the perimeter length. In view of the nine-fold symmetry of the outer shell one would expect an arbitrary particle of the outer shell to "see" eight other particle columns around the perimeter of the cylinder. And that is exactly what one can find in the right TCF hemisphere of Fig. 5(c), which corresponds to the outer shell of the solid cluster. Since this plot only shows half the perimeter, there are four areas of high correlation at $L_{\mathrm{II}} \approx [0.11, 0.22, 0.33, 0.44]$ perimeter fractions (p.f.) due to the nine-fold symmetry. This being visible already in the C2P, the TCF gives additional insight in the intrashell structure of which some exemplary features will be described now.

The first one is the correlation gap in all TCFs in the range of the nearest neighbor distance ($d_{\mathrm{NN}} \approx 0.25$ p.f. for the first shell and $d_{\mathrm{NN}} \approx 0.1$ p.f. for the second shell) between $\Psi = 0°$ and $\Psi = 30°$. The existence of this area is evident because the second particle is chosen by the integration to be a direct neighbor so a third in the same distance at a bond angle around 0° is not possible in a strongly coupled system. Further, in the outer shell of the solid cluster [right hemisphere of Fig. 5(c)] the first high correlation areas appear in the nearest neighbor region at $\Psi \approx 45°$. This means the vertical particle columns are not interlocked in a way that forms a hexagonal structure on the cylinder surface, which would result in a bond angle of $\Psi = 60°$, but are rather aligned in a square lattice. This characteristic arises due to the final boundaries of the cluster, the strong vertical confinement and the non-commensurate number of particles to form a hexagonal lattice. In such a square lattice an arbitrary particle with an arbitrary neighbor will eventually "see" a third particle directly above, below or at same height all around the cylinder perimeter. This leads to the elongated islands of high correlation for larger L_{II} which have their center at bond angles of $\Psi \approx 0°, 90°, 180°$.

Interestingly, the inner shell shown in the left hemisphere of Fig. 5(c) does not show correlation islands at those positions. Here, they start to form at $\Psi \approx 60°, 120°, 180°$ for second and third particles of the triplet in the nearest neighbor region. Thus the inner shell does in opposition to the outer shell feature a more hexagonal than square lattice. As the cluster heats up, one can again observe the loss of long range order resulting in the blurred correlation functions shown in Fig. 5(d).

In summary, the presented modified distribution functions are well suited to investigate the intershell and intrashell cluster structure.

C. Configurational entropies

The next step is to derive the configurational entropies for each cluster temperature by using Eq. (4) and then look for indicators of a phase transition. Figure 6 shows the thermal progression of the configurational C2P entropies $S^{(2)}$ and TCF entropies $S^{(3)}$ of the 39-particle cluster and will now be described in more detail.

To compare the entropies from the different correlation functions, the curves have been normalized to their respective maximum value which is always the one at the lowest Γ. The error bars indicate a rough estimation of the data consistency. To generate them, every entropy has been calculated with only half of the data set (frames) and the difference between that and the entropy from the full data set is given as the error.

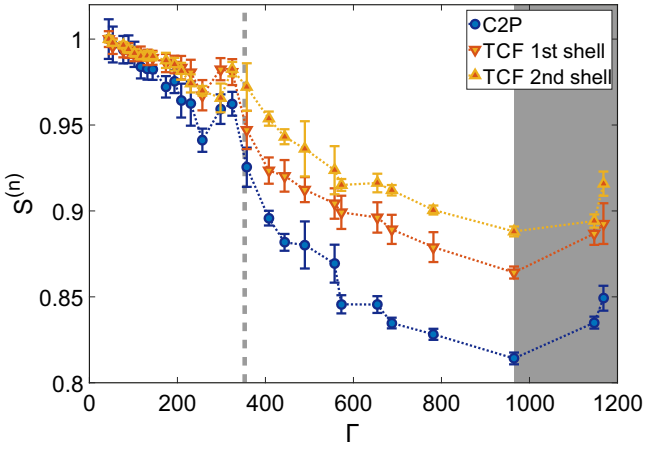

FIG. 6. Configurational entropies calculated from the C2Ps and TCFs of a 39-particle cluster. The dashed gray line indicates the derived critical coupling parameter while the grayed area marks where the cluster is in a metastable configuration.

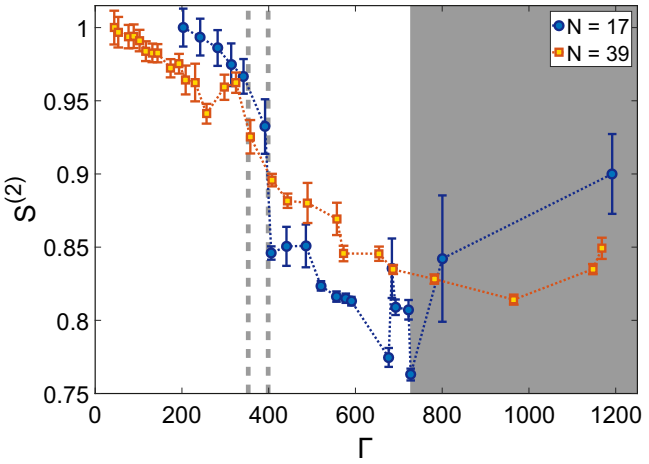

FIG. 7. Configurational entropies calculated from the C2Ps of a 17-particle cluster (blue circles) and a 39-particle cluster (yellow squares). The dashed gray lines indicate the critical coupling parameters while the grayed area marks where the 17-particle cluster is in a metastable configuration.

Starting at low temperatures the entropies calculated from the different correlation functions have their minimum at $\Gamma \approx 1000$. Then, upon heating, the entropies increase slowly. The region between $410 > \Gamma_{\mathrm{crit}} > 320$ features a steeper slope after which a region with an again decreased slope follows. We interpret the range of $\Gamma \approx 370$ as the region of phase transition due to the relatively sharp increase in entropy. The dashed gray line indicate the middle point of that region and can be identified as the critical coupling parameter Γ_{crit}. For $\Gamma < \Gamma_{\mathrm{crit}}$ the fluid range is seen, whereas for $\Gamma > \Gamma_{\mathrm{crit}}$ the solid phase is found. Finally, the grey marked area above $\Gamma \approx 1000$ indicates a region where the entropy counterintuitively again increases with Γ. This happens due to metastable configurations in which the cluster is trapped [43–45]. At these high Γ values it is difficult for the systems to reach the ground state. With enough kinetic energy, the cluster is able to "fall down" into its ground state, where the entropy is minimal. This is an effect that we were able to observe multiple times for different clusters.

The overall trend of all three curves in Fig. 6 is generally very similar. Thomsen and Bonitz however, have observed distinct differences between the $S^{(2)}$ and $S^{(3)}$ for clusters well below the melting temperature [23]. Their simulations featured additional changes in the slope of the TCFs $S^{(3)}$ for the different shells of a 80-particle cluster and identified them as the early onset of intrashell disordering. If we were able to heat up the cluster from much lower temperatures resulting in an entropy curve that spans one or two orders more of magnitude on the Γ-scale it should be possible to see this onset of intrashell-disordering as well. With the experimental setup at hand this is not possible and therefore it is well expected that the $S^{(2)}$ and $S^{(3)}$ curves are very similar. Due to this fact and since its curve features the highest dynamic range we will focus on the C2P entropies in the following analysis of different clusters.

D. Size effect

To discuss the effect of different particle numbers Fig. 7 shows the C2Ps $S^{(2)}$ entropy curves for a 17-particle cluster and the already discussed 39-particle cluster.

At the beginning (highest Γ, lowest T_{kin}) the smaller cluster is trapped in a metastable configuration as already explained in the last section. It stands out that the error bars in that area are much larger than in other regions. It turns out, that there are some particle rearrangements happening in the observation time, which is typical for a cluster that is not in its ground state. The repetition timescale for those rearrangements is almost as large as the observation time. Thus, by bisecting the frames for the error estimation they happen mainly in one of the data halves resulting in much different derived entropies. This shows that a much larger observation time would be needed for a cold cluster to attenuate the effect of metastable configurations. But since our main focus lies in the identification of the phase transition this is a negligible effect.

Looking into the phase transition it is apparent that the small cluster has a very distinct and sharp increase in entropy, while the larger clusters transition is smoother and seems to feature a two-staged melting indicated by the drop of entropy at $\Gamma \approx 250$. We assume that this is a side-effect of the cylindric geometry assumed for the distribution. On the one hand, the manipulation lasers are only heating along one axis resulting in an anisotropic force that elongated the cluster horizontally at higher laser powers. On the other hand a hotter cluster tends to assume a more spherical shape because the force of the ion wind forming the chains in the solid state becomes less dominant. Nevertheless, the phase transition is clearly identified for both clusters.

Figure 8 shows the critical temperature derived from the experiments for four clusters with particle numbers of 17, 18, 39, and 72 particles. One can see, as a general trend, that the critical temperature increases with the particle number. This effect has already been seen by Schiffer [18] in his simulations. He proposes a linear dependency between the ratio of particles on the outer shell of a Coulomb cluster and the transition temperature. This linear trend is drawn together with our experimental data. The blue circles indicate the transition temperatures of the four Yukawa balls with 16/17,

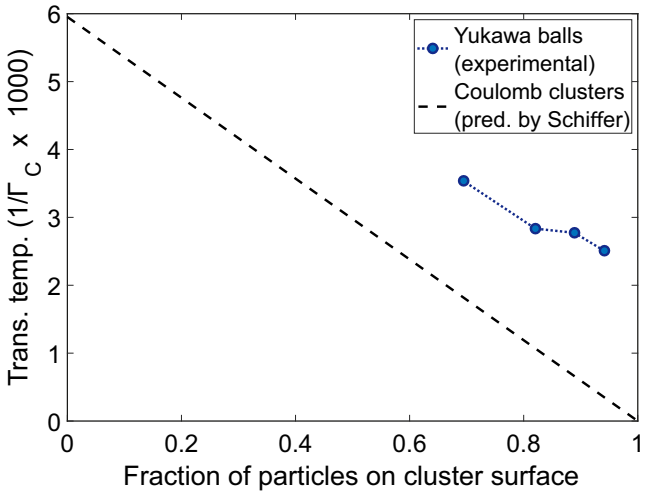

FIG. 8. Cluster size effect on the transition temperature of four different clusters ($N = 17,18,39,72$) compared to the predicted curve for Coulomb clusters by Schiffer [18].

16/18, 32/39, and 50/72 particles on their outer shells. Our experiments show a very similar linear trend but the absolute transition temperatures are a factor of 1.5 above Schiffer's predicted curve. Including the effect of shielding would result in even larger distance between our experimental data and Schiffer's line.

There are some reasons that we believe lead to the rather large difference between Schiffer's simulations and our experiments. First, the calculated coupling parameters highly depend on the particle charge [see Eq. (1)]. The particle charge is determined as $Z \approx 3400 \pm 530$ from our normal mode analysis. Hence, the Γ_{crit} is uncertain to about 30% which would just come close to Schiffer's trend line. This error in Γ is the absolute error for all four clusters, the relative error between the experiments is much smaller since they have been performed under identical conditions.

Another question is, whether Schiffer's predicted linear trend holds true towards very low particle numbers. The smallest cluster Schiffer simulated had 100 particles and was already somewhat above his linear approximation with a larger error bar than the bigger clusters. It is possible that the linear trend only holds true for particle numbers above 100. Our clusters are all below 100 particles. For such small clusters effects of "magical numbers" (clusters with certain particle numbers, that are more stable due to a symmetrical particle configuration) come into play as well. Apolinario and Peeters [46] showed that such "magical numbers" do exist for spherical, two-shelled Yukawa balls and that the transition temperature is much higher for those configurations compared to non-magical clusters of similar size. The particle numbers of our investigated cluster are different from Apolinario's. However due to the different geometry (cylindrical instead of spherical and additional wake-field influence) certain very stable configurations might exist for other particle numbers. To evaluate this a finer variation of particle number would be necessary which is beyond the scope of this article. Our observed dependency between cluster size and transition temperature does not hint toward very stable configurations yet.

Summarizing, we observe a clear size dependence of the phase transition using cylindrical correlation functions to measure a statistical configurational entropy.

V. CONCLUSION

Our experiments showed that the usage of correlation functions as proposed by Thomsen and Bonitz [23] are highly suitable for evaluation of structural properties and determination of phase transitions of finite Yukawa balls. Furthermore, it is possible to adapt the original spherical correlation functions to anisotropic confinement properties leading to symmetries like the cylindrical we presented, which confirms the robustness of the approach. Using multiple cluster sizes we were able to find a clear dependence between cluster size and melting temperature. Larger clusters need more kinetic energy thus a higher temperature to break up the inner bonds and change into another phase state which is in agreement with the findings of Schiffer [18] for Coulomb clusters.

ACKNOWLEDGMENT

We gratefully acknowledge financial support by DFG under SFB-TR24, Project No. A3.

[1] M. Hoare and P. Pal, Adv. Phys. **20**, 161 (1971).
[2] T. L. Beck, J. Jellinek, and R. S. Berry, J. Chem. Phys. **87**, 545 (1987).
[3] D. D. Frantz, J. Chem. Phys. **115**, 6136 (2001).
[4] J. Duran, *Sands, Powders, and Grains* (Springer, New York, 2000).
[5] P. K. Shukla, Phys. Plasmas **8**, 1791 (2001).
[6] *Introduction to Complex Plasmas*, edited by M. Bonitz, N. Horing, and P. Ludwig (Springer, Berlin, Heidelberg, 2010).
[7] G. E. Morfill and A. V. Ivlev, Rev. Mod. Phys. **81**, 1353 (2009).
[8] O. Arp, D. Block, A. Piel, and A. Melzer, Phys. Rev. Lett. **93**, 165004 (2004).
[9] B. M. Annaratone, T. Antonova, D. D. Goldbeck, H. M. Thomas, and G. E. Morfill, Plasma Phys. Controlled Fusion **46**, B495 (2004).
[10] O. Arp, D. Block, M. Klindworth, and A. Piel, Phys. Plasmas **12**, 122102 (2005).
[11] A. Melzer, B. Buttenschn, T. Miksch, M. Passvogel, D. Block, O. Arp, and A. Piel, Plasma Phys. Controlled Fusion **52**, 124028 (2010).
[12] M. Bonitz, D. Block, O. Arp, V. Golubnychiy, H. Baumgartner, P. Ludwig, A. Piel, and A. Filinov, Phys. Rev. Lett. **96**, 075001 (2006).
[13] D. Block, M. Kroll, O. Arp, A. Piel, S. Kding, Y. Ivanov, A. Melzer, C. Henning, H. Baumgartner, P. Ludwig, and M. Bonitz, Plasma Phys. Controlled Fusion **49**, B109 (2007).
[14] S. Ichimaru, Rev. Mod. Phys. **54**, 1017 (1982).
[15] H. Ikezi, Phys. Fluids **29**, 1764 (1986).
[16] O. S. Vaulina and S. A. Khrapak, J. Exp. Theor. Phys. **90**, 287 (2000).

[17] S. Hamaguchi, R. T. Farouki, and D. H. E. Dubin, Phys. Rev. E **56**, 4671 (1997).
[18] J. P. Schiffer, Phys. Rev. Lett. **88**, 205003 (2002).
[19] J. Böning, A. Filinov, P. Ludwig, H. Baumgartner, M. Bonitz, and Y. E. Lozovik, Phys. Rev. Lett. **100**, 113401 (2008).
[20] Y. Ivanov and A. Melzer, Phys. Plasmas **12**, 072110 (2005).
[21] P. Ludwig, H. Thomsen, K. Balzer, A. Filinov, and M. Bonitz, Plasma Phys. Controlled Fusion **52**, 124013 (2010).
[22] A. Schella, T. Miksch, A. Melzer, J. Schablinski, D. Block, A. Piel, H. Thomsen, P. Ludwig, and M. Bonitz, Phys. Rev. E **84**, 056402 (2011).
[23] H. Thomsen and M. Bonitz, Phys. Rev. E **91**, 043104 (2015).
[24] M. Borda, *Fundamentals in Information Theory and Coding* (Springer, Berlin, 2014).
[25] A. Schella, M. Mulsow, and A. Melzer, Phys. Plasmas **21**, 050701 (2014).
[26] M. Himpel, B. Buttenschn, and A. Melzer, Rev. Sci. Instrum. **82**, 053706 (2011).
[27] A. Melzer, M. Himpel, C. Killer, and M. Mulsow, J. Plasma Phys. **82**, 615820102 (2016).
[28] M. Himpel, Camera calibration and 3D particle tracking toolbox for MATLAB (2016).
[29] C. Wengert, M. Reeff, P. C. Cattin, and G. Szkely, *Bildverarbeitung för die Medizin* (Springer, Berlin, 2006), pp. 419–423.
[30] J.-Y. Bouguet, Camera calibration toolbox for MATLAB (2008).
[31] H. M. Thomas and G. E. Morfill, Nature **379**, 806 (1996).
[32] A. Melzer, V. A. Schweigert, I. V. Schweigert, A. Homann, S. Peters, and A. Piel, Phys. Rev. E **54**, R46 (1996).
[33] A. V. Ivlev, U. Konopka, G. Morfill, and G. Joyce, Phys. Rev. E **68**, 026405 (2003).
[34] V. A. Schweigert, I. V. Schweigert, A. Melzer, A. Homann, and A. Piel, Phys. Rev. E **54**, 4155 (1996).
[35] M. Kroll, J. Schablinski, D. Block, and A. Piel, Phys. Plasmas **17**, 013702 (2010).
[36] V. Nosenko, J. Goree, and A. Piel, Phys. Plasmas **13**, 032106 (2006).
[37] J. Schablinski, D. Block, A. Piel, A. Melzer, H. Thomsen, H. Khlert, and M. Bonitz, Phys. Plasmas **19**, 013705 (2012).
[38] H. Thomsen, H. Khlert, M. Bonitz, J. Schablinski, D. Block, A. Piel, and A. Melzer, Phys. Plasmas **19**, 023701 (2012).
[39] A. Melzer, A. Schella, T. Miksch, J. Schablinkski, D. Block, A. Piel, H. Thomsen, H. Khlert, and M. Bonitz, Contrib. Plasma Phys. **52**, 795 (2012).
[40] C. Killer, A. Schella, T. Miksch, and A. Melzer, Phys. Rev. B **84**, 054104 (2011).
[41] Y. Ivanov and A. Melzer, Phys. Rev. E **79**, 036402 (2009).
[42] V. M. Bedanov and F. M. Peeters, Phys. Rev. B **49**, 2667 (1994).
[43] S. Kding, D. Block, A. Melzer, A. Piel, H. Khlert, P. Ludwig, and M. Bonitz, Phys. Plasmas **15**, 073710 (2008).
[44] D. Block, S. Kading, A. Melzer, A. Piel, H. Baumgartner, and M. Bonitz, Phys. Plasmas **15**, 040701 (2008).
[45] S. W. S. Apolinario, B. Partoens, and F. M. Peeters, New J. Phys. **9**, 283 (2007).
[46] S. W. S. Apolinario and F. M. Peeters, Phys. Rev. E **76**, 031107 (2007).